Digital Alloy InAlAs Avalanche Photodiodes

Jiyuan Zheng , Yuan Yuan , Yaohua Tan, Yiwei Peng, Ann K. Rockwell , Seth R. Bank, *Senior Member, IEEE*, Avik W. Ghosh, *Senior Member, IEEE*, and Joe C. Campbell , *Fellow, IEEE*

Abstract—InAlAs digital alloy avalanche photodiodes exhibit lower excess noise than those fabricated from conventional random alloy material. Experiment and Monte Carlo simulation both show that relative to the random alloy the ionization probability for electrons is slightly lower while that of holes is greatly suppressed. We propose that the suppression of carrier ionization probability in digital alloys happens because of the creation of minibands that localize carriers. The difference of suppression between conduction bands and valence bands comes from the difference of scattering path.

Index Terms—III-V semiconductor materials, avalanche breakdown, monte carlo methods, photodiodes.

I. INTRODUCTION

IMPACT ionization in avalanche photodiodes (APDs) gives rise to internal gain, which has enabled improved performance in a broad range of applications including optical communications, imaging, and single photon detection [1]–[4]. For optical communications, APDs have provided higher direct detection receiver sensitivities than p-i-n photodiodes [1]. Recently, the emergence of 100 Gb/s Ethernet has spurred research on low-noise APDs with high gain-bandwidth product [1], [4]–[11]. Quantum optics and quantum communications require high-performance single photo detectors [3]. Typically, photomultiplier tubes (PMTs) have been employed for these applications owing to their high multiplication gain, extremely low noise, and relatively high response speed. However, PMTs have the disadvantages of being fragile, bulky, expensive, and requiring high bias. APDs, on the other hand, have emerged as potential candidates to replace PMTs for detection of low-level signals. They have demonstrated quantum efficiencies higher than those of PMTs and have the advantages of solid-state photodiodes in that they are small, inexpensive, and rugged.

In addition, they provide an additional degree of functionality in that they can be fabricated into detector arrays [12]–[16]. However, a primary negative feature of APDs is the excess noise that results from the random nature of impact ionization.

In an APD, both electrons and holes have the potential to generate new carriers by impact ionization. This can create positive feedback chains [12]. Random breaks in these chains can result in significant fluctuations in the gain, *M*, i.e., the number of carriers created by each primary carrier injected into the high-field multiplication region. This gives rise to noise in addition to thermal noise and shot noise [17]. Ignoring thermal noise, the noise power spectral density, Φ, can be expressed as [1].

$$\Phi = 2qIR(\omega)M^2F(M) \qquad (1)$$

where q, I and $R(\omega)$ represent electron charge, current, and device impedance, respectively. In addition to increasing the shot noise by M^2, the APD introduces the excess noise factor, *F(M)*, which reflects the random property of the gain. In the local field model the excess noise factor is given by $F(M) = kM + (1 - k)(1 - 1/M)$ [18] where $k\,(0 < k < 1)$ is the ionization coefficient ratio Between the two types of carriers. The lowest noise is achieved for low values of *k* [1], [12], [18].

There are three approaches to achieve low excess noise: (1) choosing semiconductor materials with favorable ionization coefficients; (2) scaling the multiplication region to take advantage of the non-local properties of impact ionization [17], [19]–[23]; and (3) impact ionization engineering utilizing heterojunction structures [24]–[28]. For bulk multiplication regions, the highest performance has been achieved by Si in the visible and near-infrared, and InAs and HgCdTe in the mid-infrared [1]. For the optical communication wavelengths (1.3 to 1.6 μm) In-GaAs/InAlAs and Ge/Si separate absorption, charge, and multiplication (SACM) structures have achieved the lowest noise and highest gain bandwidth products. However, InGaAs/InAlAs exhibits significantly higher noise than Si, HgCdTe or InAs and Ge/Si APDs are limited by the high dark current that arises from the lattice mismatch between Ge and Si [18].

Recently, $Al_xIn_{1-x}As_ySb_{1-y}$ digital alloy p-i-n and SACM APDs have demonstrated excess noise comparable to Si ($k = 0.01$) at 1550 nm [18], [29]–[32]. However, the physical mechanisms responsible for such low noise have not been identified. In this paper, an APD made by InAs/AlAs digital alloy was investigated. It was found that such APD also exhibits low excess noise (k = 0.01), which is much lower than the InAlAs random alloy that has been employed in SACM In-GaAs/InAlAs telecommunications APDs (k = 0.2) [33], [34].

J. Zheng, Y. Yuan, Y. Tan, Y. Peng, and J. C. Campbell are with the Electrical and Computer Engineering Department, University of Virginia, Charlottesville, VA 22904 USA (e-mail: jz8g@virginia.edu; yy6mf@virginia.edu; yt5x@virginia.edu; yp2bb@virginia.edu; jcc7s@virginia.edu).

A. K. Rockwell and Seth R. Bank are with the Microelectronics Research Center, University of Texas, Austin, TX 78758 USA (e-mail: akrockwell@utexas.edu; sbank@ece.utexas.edu).

A. W. Ghosh is with the Department of Physics and Electrical and Computer Engineering Department, University of Virginia, Charlottesville, VA 22904 USA (e-mail: ag7rq@virginia.edu).

Color versions of one or more of the figures in this paper are available online at http://ieeexplore.ieee.org.

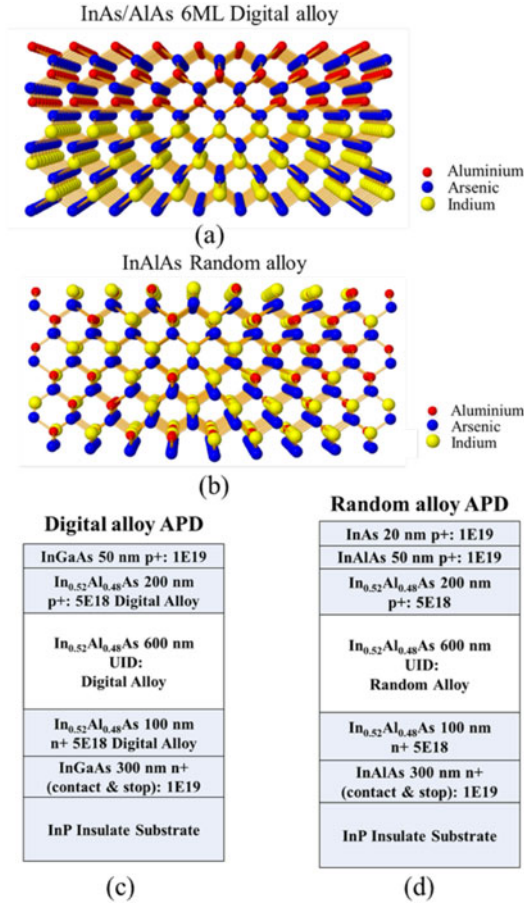Digital Object Identifier 10.1109/JLT.2018.2844114

Fig. 1. Ball & stick structure of digital alloy and random alloy and schematic diagram of their APDs. (a) Ball & stick structure of 6 ML digital alloy. (b) Ball & stick structure of random alloy. Gray, purple and brown ball represent aluminium, arsenic and indium atoms, respectively. (c) Schematic diagram of the digital alloy APD. (d) Schematic diagram of the RA APD.

In this paper, we analyze the mechanisms that contribute to low excess noise in InAlAs digital alloys.

The band structure of a 6 mono-layer (ML) InAs/AlAs digital alloy has been calculated using the tight binding method. The full band ensemble is incorporated into a Monte Carlo simulation tool to study transport behavior. It is found that the energy distribution of holes is compressed relative to the random alloy, whereas that of the electrons is relatively unchanged. It follows that hole impact ionization is suppressed, which results in lower k values and lower excess noise in the InAlAs digital alloy.

II. MATERIALS AND DEVICE PERFORMANCE

A. Lattice Structure of Digital Alloy

Fig. 1 shows ball and stick structures of digital and random alloys and schematic diagrams of the corresponding APDs. The digital alloy is a periodic structure with each period containing a small number of monolayers (ML) of each binary constituent. For example, as shown in Fig. 1(a), one period of a 6ML digital alloy of InAlAs consists of 3 monolayers of AlAs and 3 monolayers of InAs. In contrast, as shown in Fig. 1(b), the stacking of a random alloy is not periodic in the column III element.
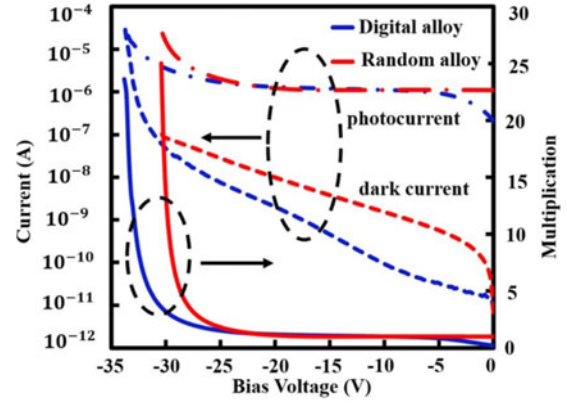

Fig. 2. Experimental result of the digital alloy and random alloy APD.

B. Growth and Fabrication

The APDs in Figs. 1(c) and 1(d) have p-i-n structures. The wafers were grown by molecular beam epitaxy. The unintentional doping densities in for the digital random alloys are $3.24 \times 10^{15}/cm^3$ and $2.08 \times 10^{15}/cm^3$, respectively, derived by C-V measurement. Although the contact layers materials for the digital alloy and random alloys are different, there will be no influence on the electric field distribution of active region because the contact layers are all heavily doped and stable ohmic contacts were achieved for both wafers. Thus, the electric field distribution in active region will not be affected. The compositions of both alloys were lattice-matched to InP. Mesa structures were defined by standard photolithography, and etched by a 1: 8: 80 solution of $H_2SO_4 : H_2O_2 : H_2O$. The top and bottom contacts are composed of 300 Å Ti and 800 Å Au. SU-8 was utilized as a passivation to reduce the surface dark current.

C. Device Measurement

A Kelthley 2400-C source meter was used to measure the current-voltage characteristics of the devices. A He-Ne tunable laser (543 nm) was used as the light source. Excess noise measurements were carried out at room temperature using an HP 8970 noise figure meter.

Fig. 2 shows dark current, photocurrent, and gain versus bias voltage. Higher bias was required for the digital alloy APD compared to the random alloy APD in order to achieve the same gain. Fig. 3(a) shows the excess noise versus gain for the digital and random alloy InAlAs APDs. For the same gain, the excess noise in the digital alloy was reduced compared with the random alloy. At a gain of 6, the excess noise factors of the random and digital alloy APDs were 2.7 and 1.6, respectively. Local-field-model curves of constant k are plotted for reference [18]. The random alloy APD exhibits k ∼ 0.2, which is consistent with published results [34]–[36].

The digital alloy approaches k = 0.01, which is similar to that reported for AlInAsSb digital alloy APDs [18], [30], [31]. As the average material compositions were essentially the same in the digital alloy and the random alloy, we conclude that the periodic structure of the digital alloy plays an important role in suppressing k.
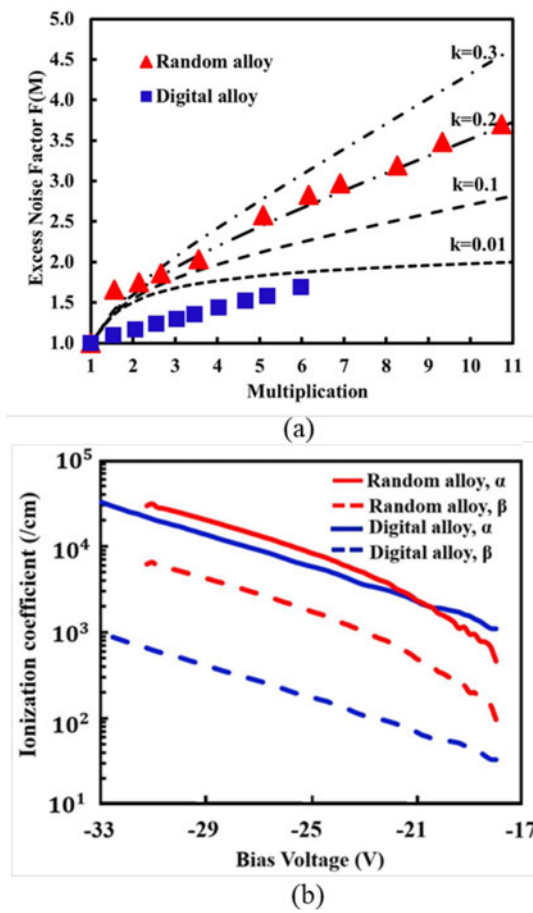
Fig. 3.   (a) Excess noise measurement and (b) ionization coefficient calculated.

The gain of an APD can be calculated using the expression [37]

$$M_n = \left\{ 1 - \int_0^W \alpha \exp\left[-\int_0^x (\alpha - \beta)\, dx' \right] dx \right\}^{-1} \quad (2)$$

where W is the thickness of multiplication region and α and β are the electron and hole ionization coefficients, respectively. For this work, equation (2) was used to estimate the ionization coefficients using the experimental data in Fig. 2 and Fig. 3(a). Fig. 3(b) shows the calculated ionization coefficients versus bias voltage. Relative to the random alloy, the hole ionization rate was significantly reduced for the digital alloy while that of the electron is approximately the same. It follows that in the digital alloy, electrons dominate the gain process, which contributes to low excess noise.

III. THEORETICAL ANALYZATION OF DIGITAL ALLOY

A. Band Structure

The tight binding method has been used to calculate the band structure of digital alloys and random alloys. The tight binding model used in this work is an environment dependent model that accounts for strain and interface-induced changes in the environment (changes in neighboring atoms, bond lengths and bond angles) of each atom in the system [38]. With the parameters
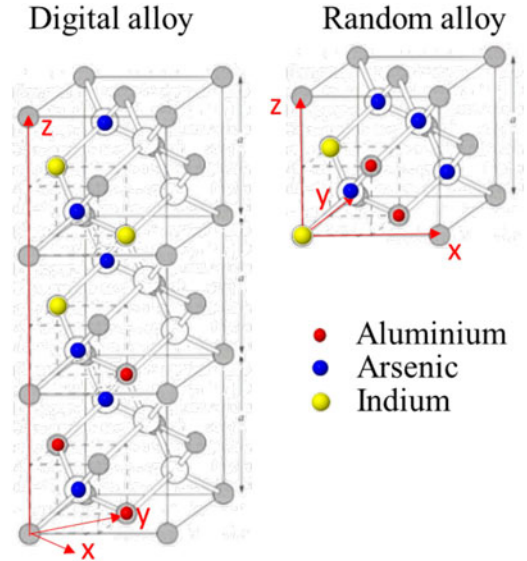

Fig. 4.   Supercell used in tight binding calculation.

calibrated with respect to the hybrid functional band structures and wave functions [39], this tight binding model has shown the capability of matching the hybrid functional band structures for bulk, strained, and superlattice materials [38]. Supercells are often created to calculate large periodic systems such as superlattices, quantum dots, and defect systems. Fig. 4 shows the supercells of InAlAs digital and random alloys in the zinc blende lattice structure. The dots in each figure denote all the atoms in a supercell. Twelve atoms were chosen as the supercell for the 6 ML digital alloy, composing of 6 As, 3 In, and 3 Al atoms. Eight atoms comprised the random alloy supercell with 4 As, 2 In, and 2 Al atoms. In both structures the In and Al compositions were 50%. According to the translational symmetry of the supercell, the first Brillouin zones of both the digital alloy and the random alloy have cubic profiles.

Figs. 5(a) and 5(b) show the E-k relationships calculated along the growth direction in the digital alloy and the random alloy, respectively. In Fig. 5(a), the E-k relationship along the growth direction ($\Gamma \rightarrow A$, $B \rightarrow C$, $D \rightarrow E$) starting from different positions (Γ, B, D) at transverse direction to growth in the first Brillouin zone are considered. Γ and D are the center and boundary of the first Brillouin zone. B is a scanning point chosen along $\Gamma \rightarrow D$ direction. In Fig. 5(a), B is set with a distance of 1/10th of the length of $\Gamma \rightarrow D$ and close to Γ. In Fig. 5(a), it can be seen that, due to the vertical quantum confinement, there are energy gaps at the boundary of the first Brillouin zone. In addition, there are minigaps between different bands, for example, as denoted by the shaded regions, there is a gap between the second and third conduction bands along the Γ-A direction and a gap between the second and third valence bands along the Γ-A direction. Since the optical phonon energy in both InAs and AlAs is below 40 meV [40], we assume the phonon energy of the InAlAs digital alloy to be the average of that in InAs and AlAs and thus the phonon energy of the InAlAs digital alloy is lower than 40 meV [40], which is less than most of the minigaps for the digital alloy. This inhibits scattering
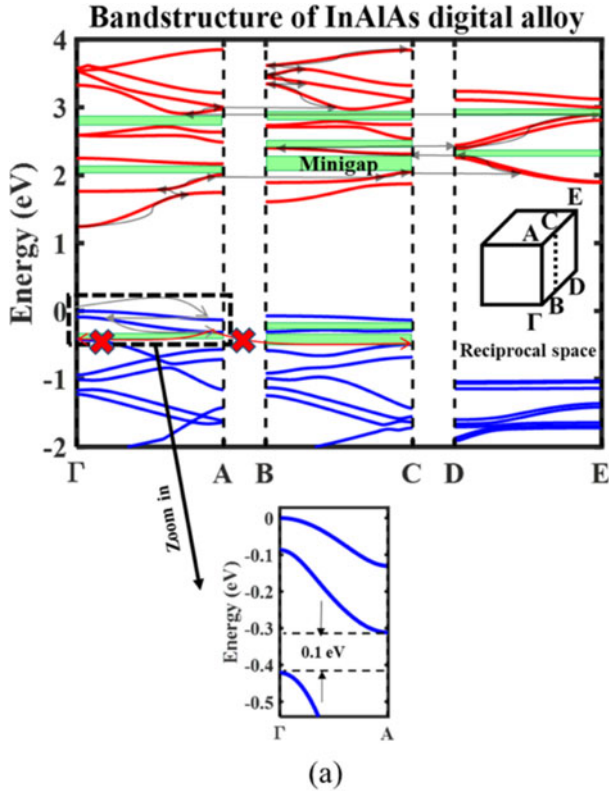
Fig. 5. Band structure calculated by tight binding method. (a) Band structure calculated for digital alloy. (b) Band structure calculated for random alloy.

Fig. 6. Carrier distribution in k-space (a) Hole (left) and electron (right) distribution in first Brillouin zone for digital alloy. (b) Hole (left) and electron (right) distribution in first Brillouin zone for random alloy.

from low-order bands to higher-order bands along the electric field direction, [001]. However, as shown in Fig. 5(a), the location and width of minigaps varies along different directions in k space. Electrons can get rid of present minigap with the help of in plane scattering and a further accelerating afterwards, for example, the arrows in the conduction band show a path by which the electron can surmount minigaps. In plane scattering plays an important role to let electron bypassing minigaps. However, when B point scanning along $\Gamma \rightarrow D$ direction, no such paths are found in valence band. The path with arrow in valence band is blocked by the minigaps. On the other hand, as can be seen in Fig. 5(b), no such energy gaps are observed in the band struc-
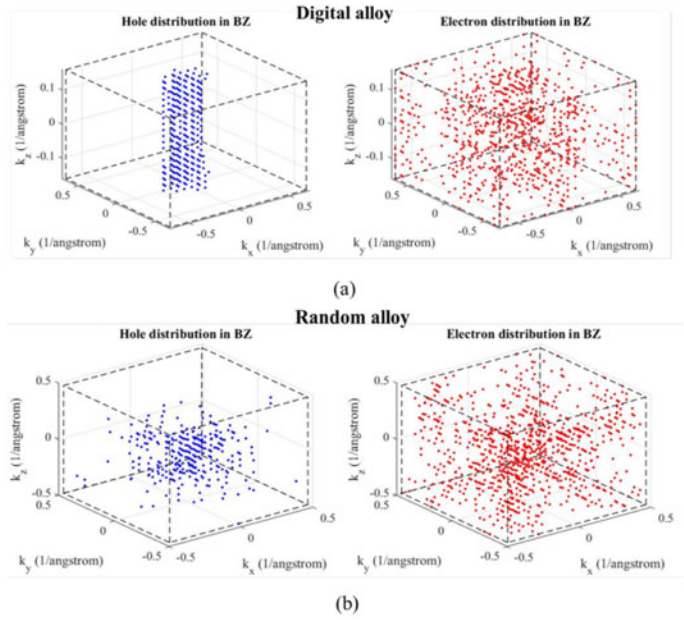
ture of the random alloy. Carriers can easily transit to high-order bands along the [001] direction as illustrated with the arrows.

Moreover, in digital alloy, since the supercell exhibits large scale in real space along the [001] direction, the scale of first Brillouin zone is small. It is relatively easy for carriers to achieve the momentum to reach the boundary of first Brillouin zone along [001] direction, which provides a foundation for Bloch oscillations (BO) to occur [41], [42].

B. Monte Carlo Simulation Results

We attribute the ionization coefficient suppression to be the result of the band structure of the digital alloy. A full band Monte Carlo simulation tool was used to study transport in the digital and random alloys. The most important scattering mechanism in III-V based material, deformation scattering, is included in the simulation. Fermi Golden rules are used to calculate the scattering rates between energy states within the whole 3D-First Brillouin Zone. Detailed model can be referred to literature [43]–[45]. A $19 \times 19 \times 19$ 3D spatial mesh is chosen in the entire first Brillouin Zone. The deformation potential was taken as 0.83 eV/Angstrom. The electric field was 800 kV/cm. Acoustic phonon energy and optical phonon energy are taken to be the average of InAs and AlAs and hold values of 36.4 meV and 16.5 meV, respectively [40].

Figure 6 shows the carrier distribution in reciprocal space. In the digital alloy, as shown in Fig. 6a, due to the minigaps, the distribution of holes is centered around the Γ point, which is quite different from the hole distribution in the random alloy, as shown in Fig. 6b. While in the digital alloy, as shown in Fig. 6a, due to the in-plane scattering-assisted transport, electrons can overcome the minigaps and occupy nearly the whole Brillouin
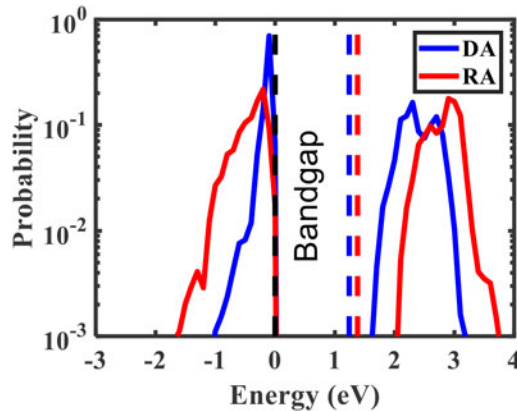
Fig. 7. Energy distribution of carriers driven by the electric field of 800 kV/cm in Digital alloy and Random alloy.

zone, which is similar to the electron distribution in the random alloy, as shown in Fig. 6b.

Figure 7 shows the energy distribution of carriers in a digital alloy and a random alloy for an electric field of 800 kV/cm. In the digital alloy, due to the minigap, the energy distribution of holes is significantly reduced compared with that in the random alloy. Only electrons achieve energy greater than the bandgap and have high probability to trigger ionizations, while it is hard for holes to gain sufficient energy to initiate ionizations. This is the origin of low k and is consistent with the lower excess noise observed for the digital alloy APDs.

IV. CONCLUSION

In conclusion, the ionization coefficient ratio k in the InAlAs digital alloy APDs is lower than that of the InAlAs random alloy, which results in lower excess noise. This phenomenon is attributed to the digital alloy structure. Band structures calculated by the tight binding method and Monte Carlo simulations show that the ionization coefficients of electrons in digital and random alloys are almost the same but the ionization coefficient for holes in the digital alloy is significantly suppressed relative to the random alloy.

ACKNOWLEDGMENT

REFERENCES

[1] J. C. Campbell, "Recent advances in avalanche photodiodes," *J. Lightw. Technol.*, vol. 34, no. 2, pp. 278–285, Jan. 2016.

[2] Y. M. Kang *et al.*, "Monolithic germanium/silicon avalanche photodiodes with 340 GHz gain-bandwidth product," *Nature Photon.*, vol. 3, pp. 59–63, Jan. 2009.

[3] B. E. Kardynal, Z. L. Yuan, and A. J. Shields, "An avalanche-photodiode-based photon-number-resolving detector," *Nature Photon.*, vol. 2, pp. 425–428, Jul. 2008.

[4] J. C. Campbell, "*Advances in photodetectors*," in *Optical Fiber Telecommunications VA: Components and Subsystems*, Burlington, MA: Academic Press, 2008, pp. 221–268.

[5] M. Nada, Y. Muramoto, H. Yokoyama, T. Ishibashi, and S. Kodama, "InAlAs APD with high multiplied responsivity-bandwidth product (MR-bandwidth product) of 168 A/W.GHz for 25 Gbit/s high-speed operations," *Electron. Lett.*, vol. 48, pp. 397–399, Mar. 2012.

[6] M. Nada, Y. Muramoto, H. Yokoyama, T. Ishibashi, and H. Matsuzaki, "Triple-mesa avalanche photodiode with inverted P-Down structure for reliability and stability," *J. Lightw. Technol.*, vol. 32, no. 8, pp. 1543–1548, Apr. 2014.

[7] M. Nada, Y. Muramoto, H. Yokoyama, N. Shigekawa, T. Ishibashi, and S. Kodama, "Inverted InAlAs/InGaAs avalanche photodiode with low-high-low electric field profile," *Jpn. J. Appl. Phys.*, vol. 51, p. 02BG03 (4 pp.) Feb. 2012.

[8] M. Nada, H. Yokoyama, Y. Muramoto, T. Ishibashi, and H. Matsuzaki, "50-Gbit/s vertical illumination avalanche photodiode for 400-Gbit/s ethernet systems," *Opt. Exp.*, vol. 22, pp. 14681–14687, Jun. 2014.

[9] M. Nada, Y. Muramoto, H. Yokoyama, T. Yoshimatsu, and H. Matsuzaki, "High-speed avalanche photodiodes for 100-Gb/s systems and beyond," in *Proc. Eur. Conf. Opt. Commun.*, 2014, pp. 1–3.

[10] M. Huang *et al.*, "Germanium on silicon avalanche photodiode," *IEEE J. Sel. Topics Quantum Electron.*, vol. 24, no. 2, pp. 1–11, Mar./Apr. 2018.

[11] M. Y. Huang *et al.*, "25 Gb/s normal incident Ge/Si avalanche photodiode," in *Proc. Eur. Conf. Opt. Commun.*, 2014, pp. 1–3.

[12] J. Y. Zheng *et al.*, "A PMT-like high gain avalanche photodiode based on GaN/AlN periodically stacked structure," *Appl. Phys. Lett.*, vol. 109, Dec. 2016, Art no. 241105.

[13] J. Y. Zheng *et al.*, "Low-temperature-dependent property in an avalanche photodiode based on GaN/AlN periodically-stacked structure," *Sci. Rep.*, vol. 6, Oct. 2016, Art no. 35978.

[14] J. Y. Zheng *et al.*, "The influence of structure parameter on GaN/AlN periodically stacked structure avalanche photodiode," *IEEE Photon. Technol. Lett.*, vol. 29, no. 4, pp. 2187–2190, Dec. 2017.

[15] J. Y. Zheng *et al.*, "Theoretical study on interfacial impact ionization in AlN/GaN periodically stacked structure," *Appl. Phys. Exp.*, vol. 10, p. 071002 (4 pp.), Jul. 2017.

[16] J. Y. Zheng, L. Wang, Z. B. Hao, Y. Luo, L. X. Wang, and X. K. Chen, "A GaN p-i-p-i-n ultraviolet avalanche photodiode," *Chinese Phys. Lett.*, vol. 29, p. 097804 (3 pp.), Sep. 2012.

[17] M. M. Hayat, B. E. A. Saleh, and M. C. Teich, "Effect of dead space on gain and noise of double-carrier-multiplication avalanche photodiodes," *IEEE Trans. Electron Devices*, vol. 39, no. 3, pp. 546–552, Mar. 1992.

[18] S. R. Bank *et al.*, "Avalanche photodiodes based on the AlInAsSb materials system," *IEEE J. Sel. Topics Quantum Electron.*, vol. 24, no. 2, pp. 1–7, Mar./Apr. 2018.

[19] X. W. Li, X. G. Zheng, S. L. Wang, F. Ma, and J. C. Campbell, "Calculation of gain and noise with dead space for GaAs and AlxGa1-xAs avalanche photodiode," *IEEE Trans. Electron Devices*, vol. 49, no. 7, pp. 1112–1117, Jul. 2002.

[20] J. C. Campbell, S. Chandrasekhar, W. T. Tsang, G. J. Qua, and B. C. Johnson, "Multiplication noise of wide-bandwidth Inp/Ingaasp/Ingaas avalanche photodiodes," *J. Lightw. Technol.*, vol. 7, no. 3, pp. 473–478, Mar. 1989.

[21] P. Yuan *et al.*, "Impact ionization characteristics of III-V semiconductors for a wide range of multiplication region thicknesses," *IEEE J. Quantum Electron.*, vol. 36, no. 2, pp. 198–204, Feb. 2000.

[22] M. A. Saleh *et al.*, "Impact-ionization and noise characteristics of thin III–V avalanche photodiodes," *IEEE Trans. Electron Devices*, vol. 48, no. 12, pp. 2722–2731, Dec. 2001.

[23] P. Yuan *et al.*, "A new look at impact ionization—Part II: Gain and noise in short avalanche photodiodes," *IEEE Trans. Electron Devices*, vol. 46, no. 8, pp. 1632–1639, Aug. 1999.

[24] P. Yuan, S. Wang, X. Sun, X. G. Zheng, A. L. Holmes, and J. C. Campbell, "Avalanche photodiodes with an impact-ionization-engineered multiplication region," *IEEE Photon. Technol. Lett.*, vol. 12, no. 10, pp. 1370–1372, Oct. 2000.

[25] O. H. Kwon *et al.*, "Optimal excess noise reduction in thin heterojunction Al$_{0.6}$Ga$_{0.4}$As-GaAs avalanche photodiodes," *IEEE J. Quantum Electron.*, vol. 39, no. 10, pp. 1287–1296, Oct. 2003.

[26] M. M. Hayat, O. H. Kwon, S. L. Wang, J. C. Campbell, B. E. A. Saleh, and M. C. Teich, "Boundary effects on multiplication noise in thin heterostructure avalanche photodiodes: Theory and experiment," *IEEE Trans. Electron Devices*, vol. 49, no. 12, pp. 2114–2123, Dec. 2002.

[27] S. Wang *et al.*, "Low-noise impact-ionization-engineered avalanche photodiodes grown on InP substrates," *IEEE Photon. Technol. Lett.*, vol. 14, no. 12, pp. 1722–1724, Dec. 2002.

[28] N. Duan *et al.*, "High-speed and low-noise SACM avalanche photodiodes with an impact-ionization-engineered multiplication region," *IEEE Photon. Technol. Lett.*, vol. 17, no. 8, pp. 1719–1721, Aug. 2005.

[29] S. J. Maddox, S. D. March, and S. R. Bank, "Broadly tunable AlInAsSb digital alloys grown on GaSb," *Crystal Growth Design*, vol. 16, pp. 3582–3586, Jul. 2016.

[30] M. Ren, S. J. Maddox, M. E. Woodson, Y. J. Chen, S. R. Bank, and J. C. Campbell, "AlInAsSb separate absorption, charge, and multiplication avalanche photodiodes," *Appl. Phys. Lett.*, vol. 108, May. 2016, Art no.191108.

[31] M. E. Woodson, M. Ren, S. J. Maddox, Y. J. Chen, S. R. Bank, and J. C. Campbell, "Low-noise AlInAsSb avalanche photodiode," *Appl. Phys. Lett.*, vol. 108, Feb. 2016, Art no. 081102.

[32] M. Ren, S. Maddox, Y. J. Chen, M. Woodson, J. C. Campbell, and S. Bank, "AlInAsSb/GaSb staircase avalanche photodiode," *Appl. Phys. Lett.*, vol. 108, Feb. 2016, Art no. 081101.

[33] T. Nakata, T. Takeuchi, I. Watanabe, K. Makita, and T. Torikai, "10 Gbit/s high sensitivity, low-voltage-operation avalanche photodiodes with thin InAlAs multiplication layer and waveguide structure," *Electron. Lett.*, vol. 36, pp. 2033–2034, Nov. 2000.

[34] T. Nakata, I. Watanabe, K. Makita, and T. Torikai, "InAlAs avalanche photodiodes with very thin multiplication layer of 0.1 μ for highspeed and low-voltage-operation optical receiver," *Electron. Lett.*, vol. 36, pp. 1807–1809, Oct. 2000.

[35] C. Lenox *et al.*, "Thin multiplication region InAlAs homojunction avalanche photodiodes," *Appl. Phys. Lett.*, vol. 73, pp. 783–784, Aug. 1998.

[36] Y. L. Goh *et al.*, "Excess avalanche noise in In0.52Al0.48As," *IEEE J. Quantum Electron.*, vol. 43, no. 6, pp. 503–507, Jun. 2007.

[37] A. Spinelli and A. L. Lacaita, "Mean gain of avalanche photodiodes in a dead space model," *IEEE Trans. Electron Devices*, vol. 43, no. 1, pp. 23–30, Jan. 1996.

[38] Y. H. Tan, M. Povolotskyi, T. Kubis, T. B. Boykin, and G. Klimeck, "Transferable tight-binding model for strained group IV and III-V materials and heterostructures," *Phys. Rev. B*, vol. 94, Jul. 2016, Art no. 045311.

[39] Y. H. P. Tan, M. Povolotskyi, T. Kubis, T. B. Boykin, and G. Klimeck, "Tight-binding analysis of Si and GaAs ultrathin bodies with subatomic wave-function resolution," *Phys. Rev. B*, vol. 92, Aug. 2015, Art no. 085301.

[40] L. Lindsay, D. A. Broido, and T. L. Reinecke, "Ab initio thermal transport in compound semiconductors," *Phys. Rev. B*, vol. 87, Apr. 2013, Art no. 165201.

[41] C. Zener, "A theory of the electrical breakdown of solid dielectrics," in *Proc. Roy. Soc. A*, 1934, vol. 145, pp. 523–529.

[42] F. Bloch, "Über die Quantenmechanik der Elektronen in Kristallgittern," *Zeitschrift für Physik*, vol. 52, pp. 555–600, Jul. 1929.

[43] I. H. Oguzman, E. Bellotti, K. F. Brennan, J. Kolnik, R. P. Wang, and P. P. Ruden, "Theory of hole initiated impact ionization in bulk zincblende and wurtzite GaN," *J. Appl. Phys.*, vol. 81, pp. 7827–7834, Jun. 1997.

[44] S. Yamakawa, S. Aboud, M. Saraniti, and S. M. Goodnick, "Fast Full-Band device simulator for wurtzite and zincblende GaN MESFET Using a cellular monte carlo method," *J. Comput. Electron.*, vol. 2, pp. 481–485, Dec. 2003.

[45] K. Kodama, H. Tokuda, and M. Kuzuhara, "A model for calculating impact ionization transition rate in wurtzite GaN for use in breakdown voltage simulation," *J. Appl. Phys.*, vol. 114, Jul. 2013, Art no. 044509.

Authors' biographies not available at the time of publication.